

Electronic Supplementary Information

Synthesis of F-doped high-entropy layered oxide as cathode material towards high-performance Na-ion batteries

Minghui Cao,^{*a} Miao Cui,^a Yiping Gong,^a Zewei Guo,^a Shuangqing Le,^a Yangjinhua Wu,^a
Chong Lin,^a Ke Li,^a Jingyang Tian^{*a} and Yi Qi^{*b}

^aJiangxi Province Key Laboratory of Functional Organic Polymers, School of Chemistry and
Materials, East China University of Technology, Nanchang, 330013, China

E-mail: mhcao@ecut.edu.cn

E-mail: jytian2012@163.com

^bKey Lab of Separation Science for Analytical Chemistry, Dalian Institute of Chemical
Physics, Chinese Academy of Sciences, Dalian 116023, China.

E-mail: qi yi@dicp.ac.cn

Experimental and Computational Methods

Experimental Section

Material synthesis

The synthesis of P2-Na_{0.66}Mn_{0.6}Li_{0.1}Ti_{0.1}(MgAlCuZn)_{0.05}O_{2-x}F_x ($x=0, 0.1, 0.2, 0.3, 0.4$) was conducted using a conventional solid-state reaction method. A stoichiometric amount of Na₂CO₃ (99.99%, Aladdin), NaF (99.99%, Aladdin), MnO₂ (99.99%, Aladdin), Li₂CO₃ (99.99%, Aladdin), TiO₂ (99.99%, Aladdin), MgO (99.99%, Aladdin), Al₂O₃ (99.99%, Aladdin), CuO (99.99%, Aladdin), and ZnO (99.99%, Aladdin), were dispersed in anhydrous ethanol (>99.9%, Aladdin) to ensure homogeneity. A planetary ball mill was employed to mix the precursors with a ball-to-powder weight ratio of 10:1 at a rotational speed of 600 rpm for a duration of 4 hours. The resulting slurry was then dried overnight at 75 °C to yield a precursor powder. Calcination of the precursor was performed at 900 °C in an O₂ atmosphere for 12 hours. Upon cooling to room temperature, the calcined powder was immediately transferred into an Ar-filled glove box to prevent exposure to air. For comparison, the P2-Na_{0.66}Mn_{0.6}Li_{0.1}Ti_{0.1}(MgAlCuZn)_{0.05}O₂ powder without F doping was also synthesized using similar method.

Material characterization

The X-ray diffraction (XRD) patterns of synthesized powders and cycled electrodes were obtained by a Bruker D8 Advance X-ray diffractometer with Cu-K α radiation. The morphologies and energy-dispersive spectroscopy (EDS) were obtained through scanning electron microscopy (SEM, TESCAN MIRA LMS) and field-emission transmission electron microscopy (TEM, JEOL JEM-2100F), respectively. For the vibrational spectroscopy study, FTIR (Thermo Fisher Scientific Nicolet iS20) and Raman (Thermo Scientific DXR, 532nm) spectrometers were employed. The Mn 2p, O 1s and F 1s XPS spectra of the samples were collected by a PerkinElmer PHI 5000C electron spectrometer using monochromatic Al K α X-ray source. Binding energies (BEs) of Mn, O and F elements in samples were calibrated relative to the carbon C 1s peak (~284.6 eV).

Electrochemical characterization

P2-Na_{0.66}Mn_{0.6}Li_{0.1}Ti_{0.1}(MgAlCuZn)_{0.05}O_{2-x}F_x electrodes are composed of 70 wt % P2-Na_{0.66}Mn_{0.6}Li_{0.1}Ti_{0.1}(MgAlCuZn)_{0.05}O_{2-x}F_x material, 20 wt % carbon black (Super P) and 10 wt % polyvinylidene fluoride (PVDF) binder. The electrodes were dried overnight under vacuum at 80 °C and punched to a disk shape with a diameter of 12 mm before half-cell fabrication. The mass loadings of the active materials on each working electrode are ~ 3 mg cm⁻². The coin-type (CR2032) cells were assembled in a dry glovebox filled with high purity argon gas (H₂O < 0.1 ppm, O₂ < 0.1 ppm), for which Na metal was used as the anode, P2-Na_{0.66}Mn_{0.6}Li_{0.1}Ti_{0.1}(MgAlCuZn)_{0.05}O_{2-x}F_x was used as the cathode, and the glass fiber GF/F (Whatman) was used as the separator. The electrolyte was 1.0 M NaClO₄ (Alfa-Aesar) dissolved in a nonaqueous solution of propylene carbonate (PC, Alfa-Aesar) with 5 wt % fluoroethylene carbonate (FEC) additive. The full cell was assembled with HEOF-3 as the cathode and hard carbon as the anode. To eliminate the low initial Coulombic efficiency of hard carbon and HEOF-3, both cathode and anode were precycled. Typical mass loading of the cathodes used in this study ranges from 2.4 to 4.0 mg cm⁻² for full cells. In order to balance the capacity between cathode and anode in a full cell, the cathode capacity was 1.2 times that of the anode (The loading mass of the hard carbon electrode was controlled between 1.2 and 2.0 mg cm⁻²). After assembly, the full cells were activated for 1 cycle with low current density (0.02C, 4 mA g⁻¹) and then allowed to rest for 24 h. The galvanostatic cycling and galvanostatic intermittent titration technique (GITT) tests were conducted on a Neware cyler in the voltage range of 1.5-4.5 V (vs. Na⁺/Na) at room temperature. Cyclic voltammetry (CV) was performed on a CHI660D electrochemical working station at a scan rate of 0.1 mV/s. Electrochemical impedance spectroscopy (EIS) was performed on a CHI660D electrochemical working station in 1Hz-100KHz.

Computational Section

Na Migration Barriers

First-principles density functional theory (DFT) calculations were performed using the Vienna Ab initio Simulation Package (VASP) with the projector augmented wave (PAW) method. The

exchange-functional was treated within the generalized gradient approximation (GGA) employing the Perdew-Burke-Ernzerhof (PBE) functional. A plane wave basis set with an energy cutoff of 500 eV was employed, and the geometry relaxation was performed until the forces on each atom were below 0.05 eV/Å. The Brillouin zone was sampled using a $1 \times 1 \times 1$ k-point grid. Self-consistent calculations were conducted with an energy convergence threshold of 10^{-5} eV. The migration energy barrier is calculated by CI-NEB.

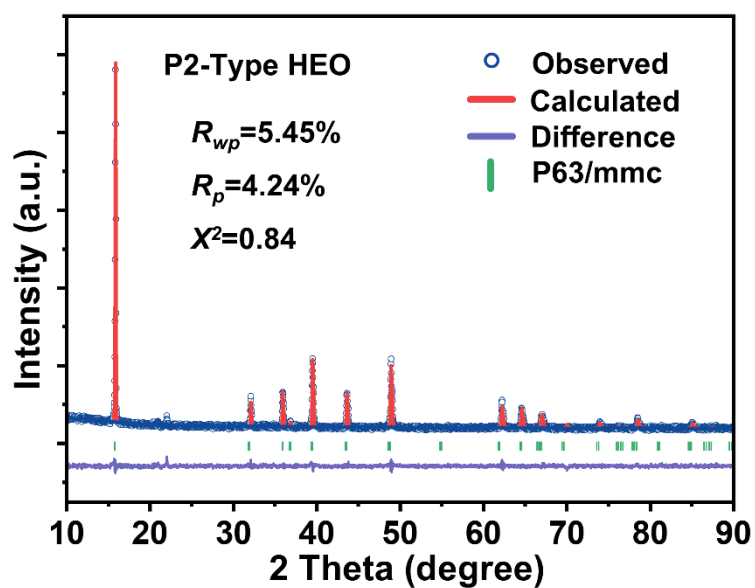


Fig. S1 (a) Rietveld refinement of the XRD profile of $\text{Na}_{0.66}\text{Mn}_{0.6}\text{Li}_{0.1}\text{Ti}_{0.1}(\text{MgAlCuZn})_{0.05}\text{O}_2$ (HEO). Dark blue circle: observed, red line: calculated, black line: background, purple line: difference and green bars: Bragg positions.

Table S1. Refined crystallographic parameters of $\text{Na}_{0.66}\text{Mn}_{0.6}\text{Li}_{0.1}\text{Ti}_{0.1}(\text{MgAlCuZn})_{0.05}\text{O}_2$ (HEO) with the Rietveld method. S.G. $P63/mmc$, $a = b = 2.88(6)$ Å, $c = 11.16(0)$ Å, $\alpha = \beta = 90^\circ$, $\gamma = 120^\circ$, $R_{wp}=5.45\%$, $\chi^2 = 0.84$.

Sample	Atom	Site	x	y	z	Occupancy
NMLTMACZ	Mn	2a	0	0	0	0.589(7)
	Li	2a	0	0	0	0.112(3)
	Ti	2a	0	0	0	0.098(2)
	Mg	2a	0	0	0	0.047(8)
	Al	2a	0	0	0	0.051(3)
	Cu	2a	0	0	0	0.053(2)
	Zn	2a	0	0	0	0.047(6)
	Na1	2b	0	0	0.25	0.328(4)
	Na2	2d	0.3333	0.6667	0.75	0.332(6)
	O	4f	0.3333	0.6667	0.0872	1
$P63/mmc : a = b = 2.8859(3)$ Å $c = 11.1596(4)$ Å $V = 80.49(2)$ Å ³ $d_{(002)} = 5.6048$ Å $R_p = 4.24\%$ $R_{wp} = 5.45\%$ $\text{GOF}(\chi^2) = 0.84$						

Table S2. Refined crystallographic parameters of $\text{Na}_{0.66}\text{Mn}_{0.6}\text{Li}_{0.1}\text{Ti}_{0.1}(\text{MgAlCuZn})_{0.05}\text{O}_{1.7}\text{F}_{0.3}$ (HEOF-3) with the Rietveld method. S.G. $P63/mmc$, $a = b = 2.89(9) \text{ \AA}$, $c = 11.28(0) \text{ \AA}$, $\alpha = \beta = 90^\circ$, $\gamma = 120^\circ$, $R_{wp}=6.53\%$, $\chi^2 = 1.46$.

Sample	Atom	Site	x	y	z	Occupancy
HEOF-3	Mn	2a	0	0	0	0.603(7)
	Li	2a	0	0	0	0.105(3)
	Ti	2a	0	0	0	0.097(2)
	Mg	2a	0	0	0	0.048(8)
	Al	2a	0	0	0	0.050(3)
	Cu	2a	0	0	0	0.051(2)
	Zn	2a	0	0	0	0.049(6)
	Na1	2b	0	0	0.25	0.324(4)
	Na2	2d	0.3333	0.6667	0.75	0.336(6)
	O	4f	0.3333	0.6667	0.0872	0.852(3)
F	4f	0.3333	0.6667	0.0872	0.147(8)	
$P63/mmc : a = b = 2.8995(3) \text{ \AA} \quad c = 11.2795(4) \text{ \AA} \quad V = 82.12(3) \text{ \AA}^3$ $d_{(002)} = 5.6545 \text{ \AA}$ $R_p = 4.49\% \quad R_{wp} = 6.53\% \quad \text{GOF}(\chi^2) = 1.46$						

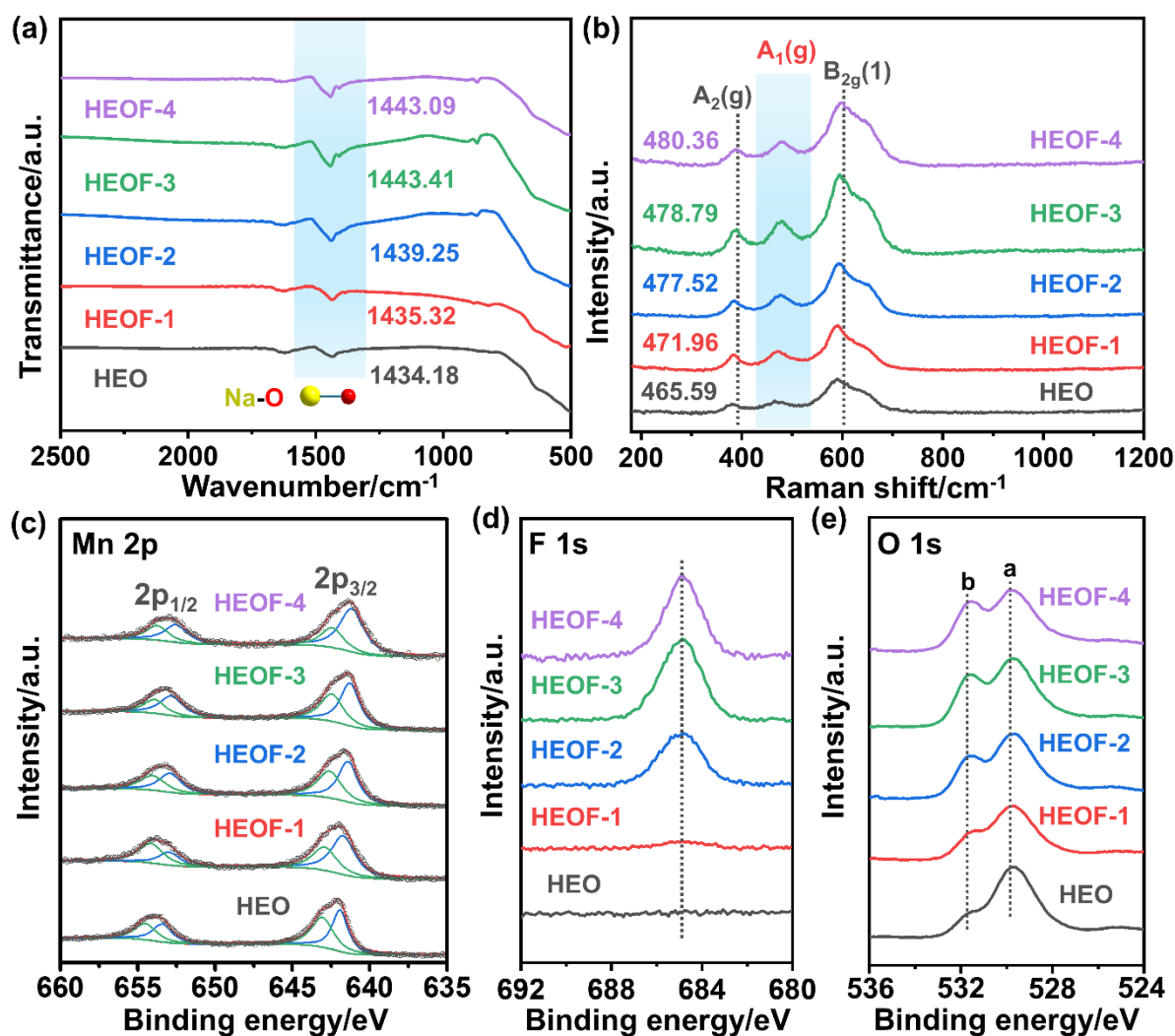


Fig. S2 (a) FTIR, (b) Raman, and (c-e) Mn 2p, F1s and O1s XPS spectra of the synthesized HEO, HEOF-1, HEOF-2, HEOF-3, and HEOF-4 samples.

Note that the presence of a higher concentration of oxygenated deposited species in F-doped materials (peak b in Fig. S2e) may have profound and diverse impacts on their electronic structure, structural stability, and surface chemical properties.^{S1-S3} Collectively, these changes can significantly influence the overall performance of the materials.

Table S3 The Mn³⁺/Mn⁴⁺ ratios in the Mn 2p XPS spectra of the synthesized HEO, HEOF-1, HEOF-2, HEOF-3, and HEOF-4 samples.

Sample	HEO	HEOF-1	HEOF-2	HEOF-3	HEOF-4
Mn ³⁺	50.09%	53.33%	54.85%	58.24%	65.42%
Mn ⁴⁺	49.91%	46.67%	45.15%	41.76%	34.58%

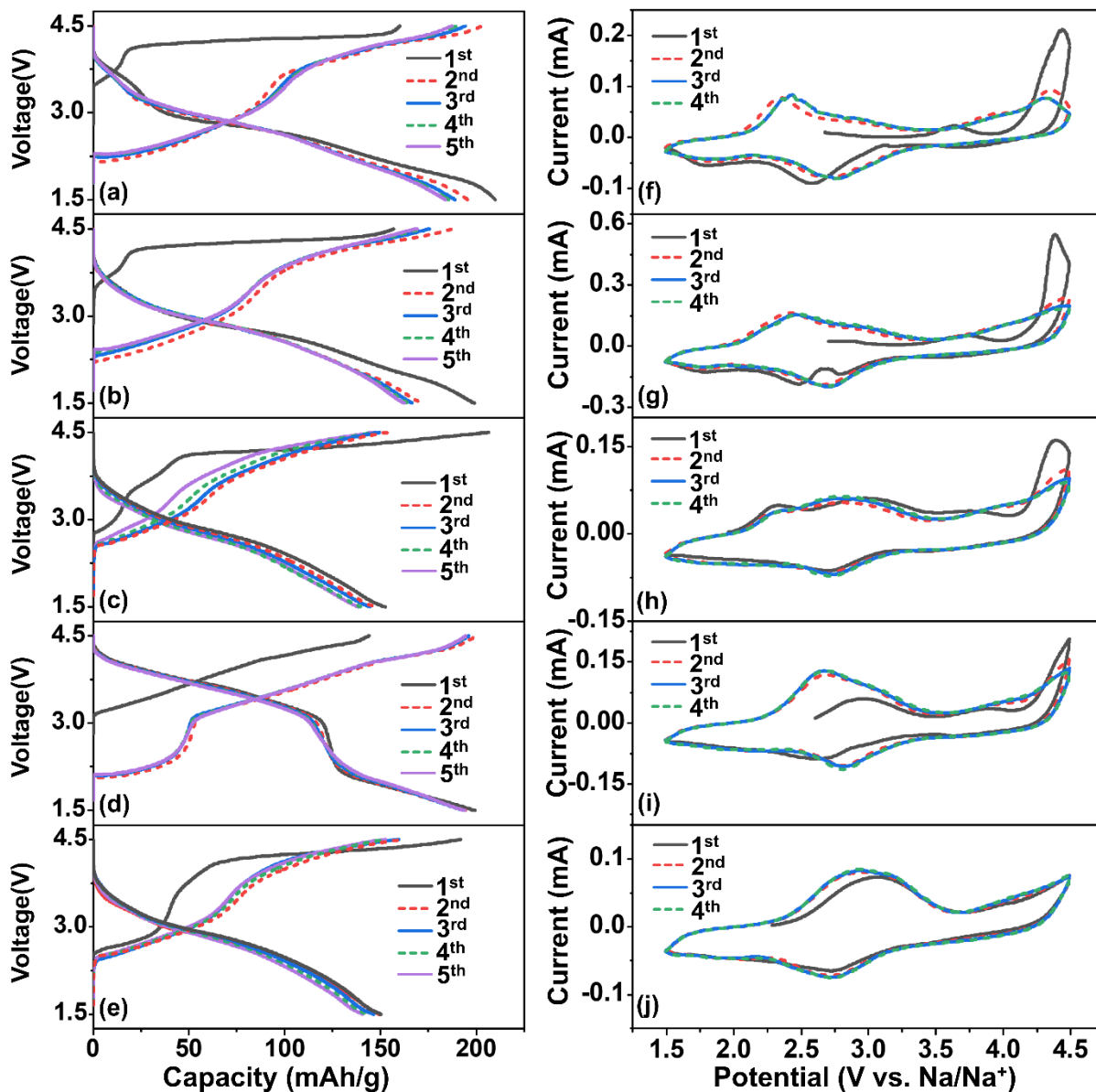


Fig. S3 The initial five galvanostatic charge/discharge profiles of the (a) HEO, (b) HEOF-1, (c) HEOF-2, (d) HEOF-3, and (e) HEOF-4 electrodes at a current rate of 0.1C in the potential range of 1.5-4.5 V versus Na⁺/Na. The CV curves of the (f) HEO, (g) HEOF-1, (h) HEOF-2, (i) HEOF-3, and (j) HEOF-4 electrodes collected within the voltage range of 1.5-4.5 V at a scan rate of 0.1 mV/s.

It is noteworthy that HEOF-2 and HEOF-4 exhibit higher reversibility in the oxygen redox reactions, yet they possess lower discharge capacities compared to other samples. This seemingly counterintuitive behavior may be attributed to improper fluorine doping, which may introduce structural defects, diminish the material's electrical conductivity, disrupt the

stoichiometric balance, and increase the likelihood of side reactions.^{S4-S6} Moreover, while fluorine doping can enhance the reversibility of the oxygen redox reaction, it may simultaneously restrict the reaction's activity.^{S7} Consequently, the capacity contribution from the oxygen redox reaction is diminished, ultimately resulting in a decline in the overall discharge capacity. Additionally, the number and intensity of redox pairs observed in the differential capacity versus voltage curves (dQ/dV) can, to some extent, elucidate the reasons for the differing capacities among the various F-doped samples (see Fig. S4).

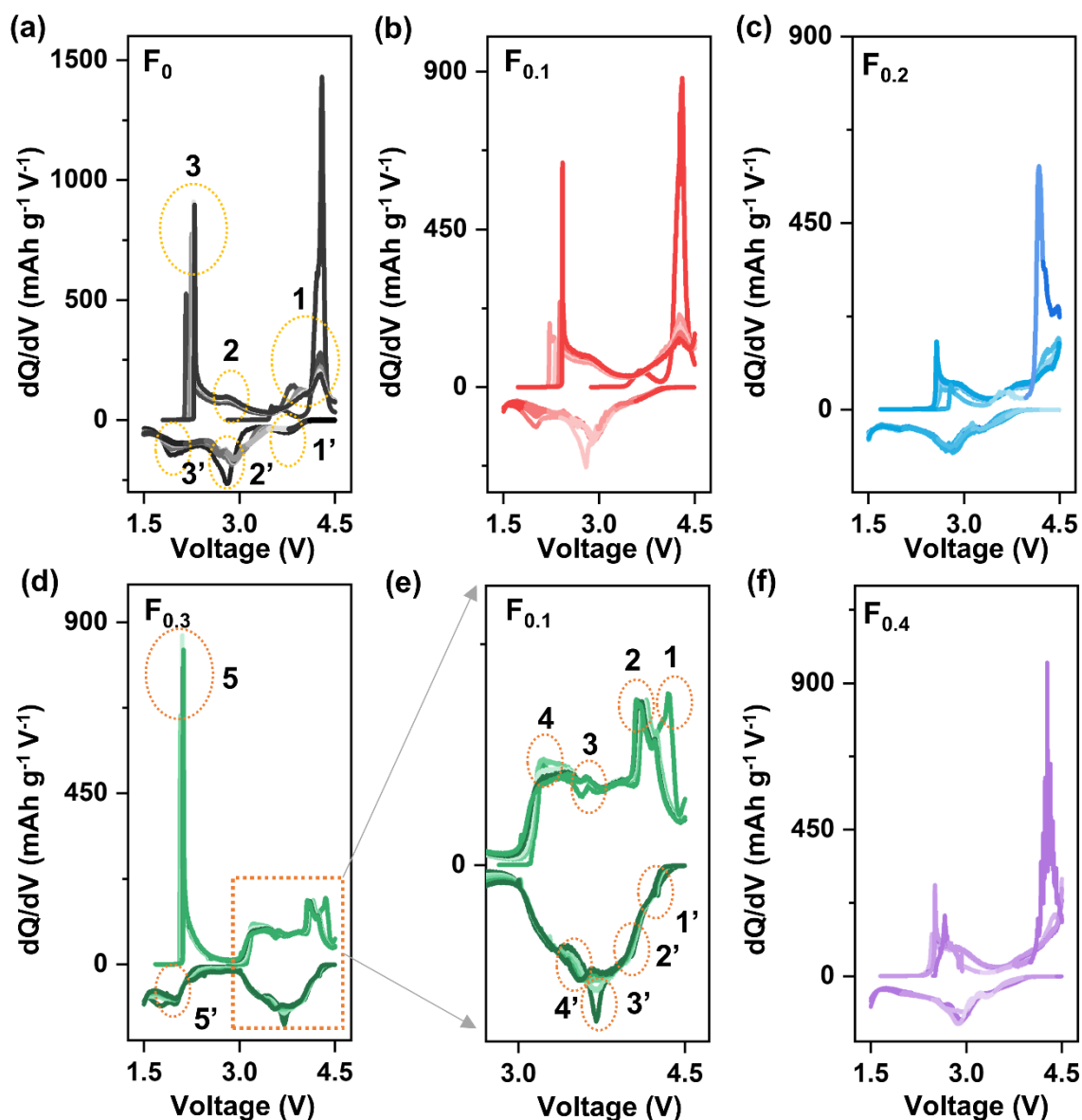


Fig. S4. The differential capacity curves corresponding to Fig.S3a-e.

In order to more clearly identify the impact of F substitution on the characteristics of charge-discharge curves, the differential capacity versus voltage curves (dQ/dV) were extracted from the initial charge-discharge curves of HEO, HEOF-1, HEOF-2, HEOF-3, and HEOF-4, and were presented in Fig. S4. For HEO, HEOF-1, HEOF-2, and HEOF-4, three pairs of major redox peaks can be observed, located in the voltage ranges of 1.5–2.5 V, 2.0–3.5 V, and 3.5–4.5 V (as exemplified by HEO in Fig. Sa). However, it is noteworthy that five pairs of major redox peaks can be observed in the dQ/dV curves of HEOF-3, situated in the voltage ranges of 1.5–2.5 V, 3.0–3.5 V, 3.5–4.0 V, 4.0–4.2 V, and 4.2–4.5 V (as indicated in the magnified area

of Fig. S4d (Fig. S4e)). Additionally, peaks 1–4 of HEOF-3 are separated from peak 5 by a distinct voltage gap. These features collectively render the dQ/dV curves of HEOF-3 distinct from those of the other samples, which well explains why the charge-discharge curves of the HEOF-3 sample are different from those of the other samples.

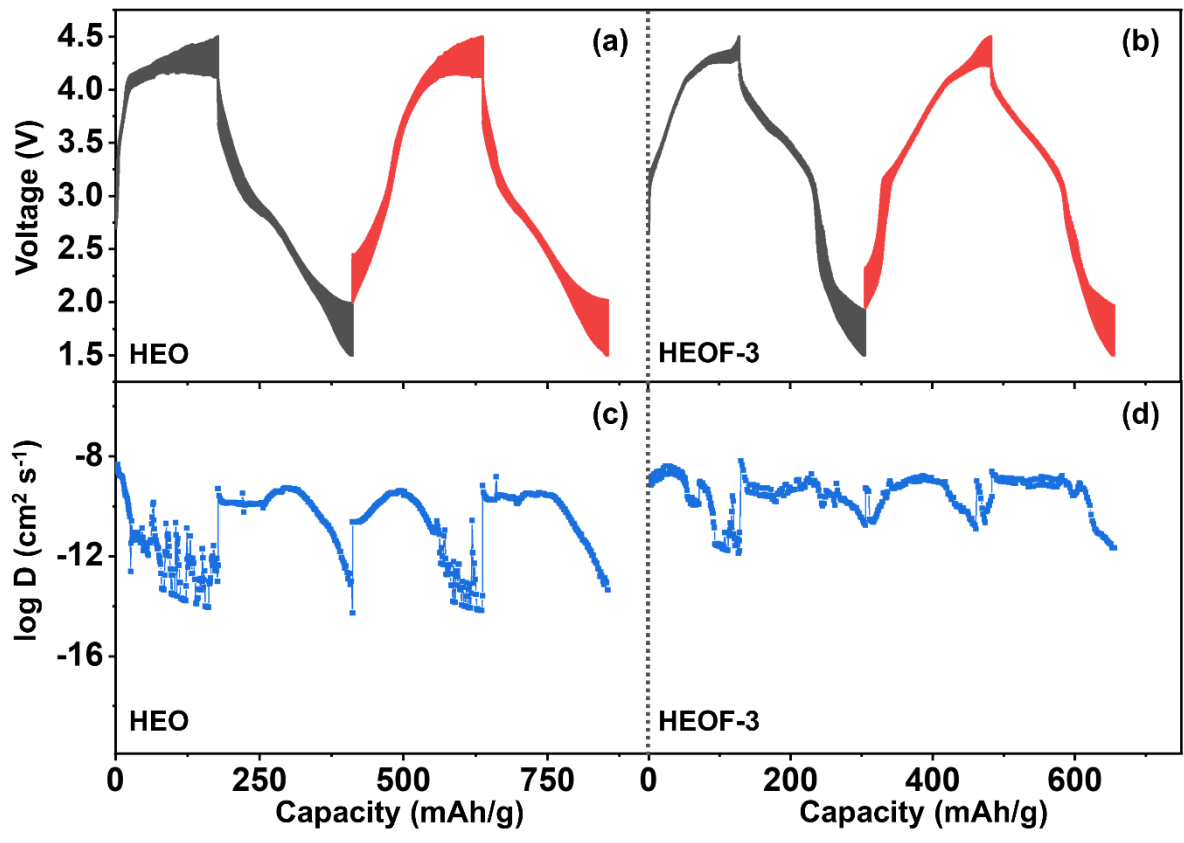


Fig. S5. The transient voltage response of (a) HEO and (b) HEOF-3 electrodes during GITT for the initial two cycles between 1.5 and 4.5 V versus Na^+/Na , Calculated D_{Na^+} values of (c) HEO and (d) HEOF-3 electrodes.

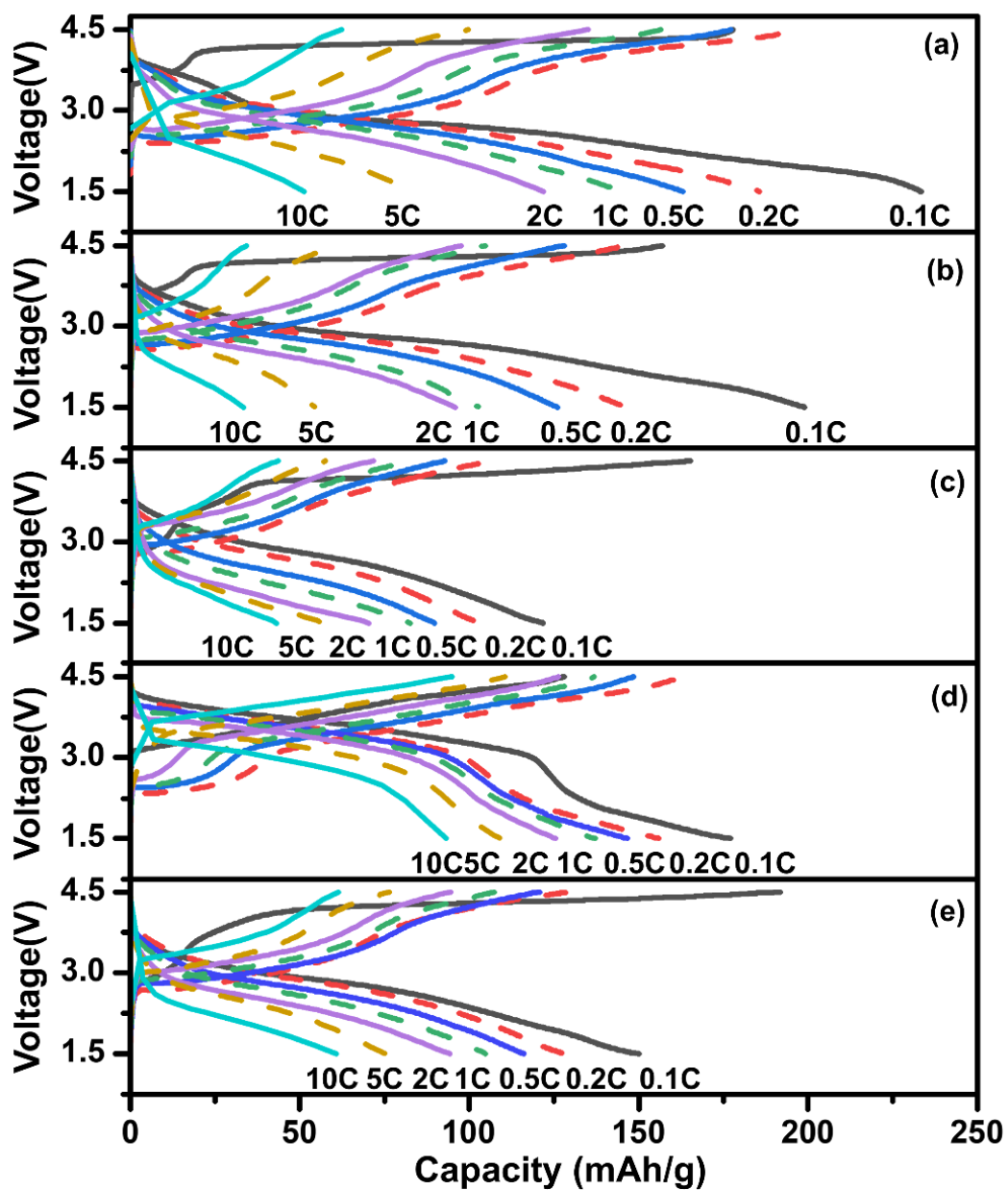


Fig. S6. The charge/discharge profiles at different current rates (0.1C-10C) of the (a) HEO, (b) HEOF-1, (c) HEOF-2, (d) HEOF-3, and (e) HEOF-4 electrodes in the voltage range of 1.5-4.5 V vs. Na^+/Na .

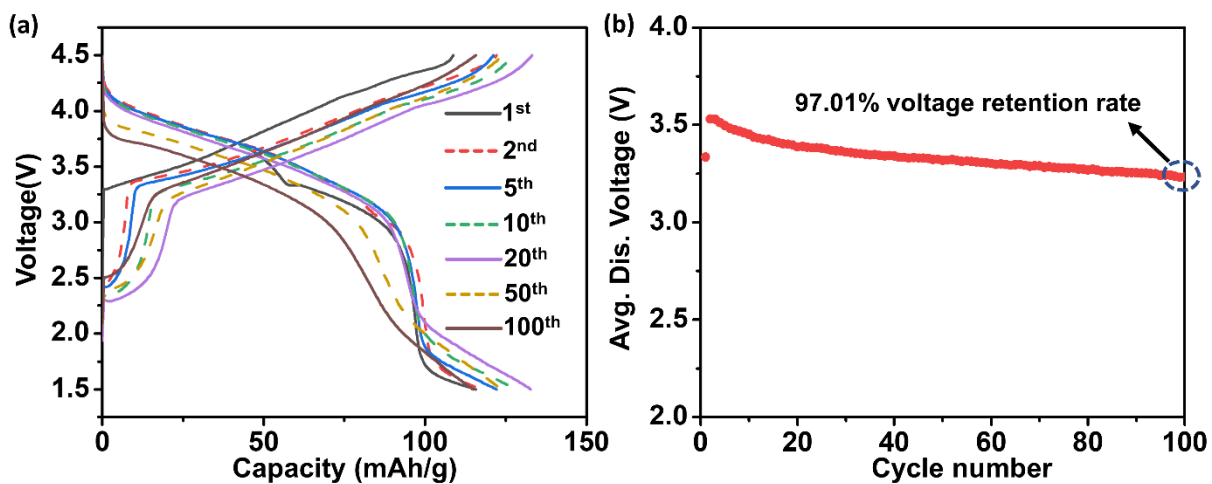


Fig. S7. (a) Typical galvanostatic charge/discharge profiles (1st, 2nd, 5th, 10th, 20th, 50th, 100th) of the HEOF-3 electrode at 1C in the voltage range of 1.5-4.5 V. (b) Average discharge voltage vs. cycle number plot of the HEOF-3 electrode within 100 cycles.

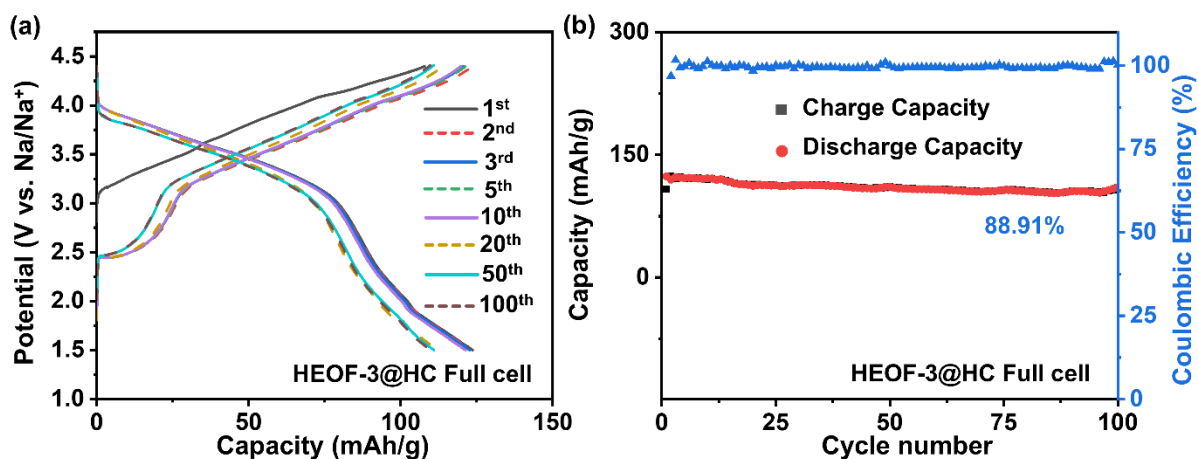


Fig. S8. (a) Typical charge/discharge curves of the HEOF-3@HC full cell cycled between 1.5 and 4.4 V at 1C rate. (d) The charge/discharge capacity and coulombic efficiency versus cycle number at the 1C rate for the HEOF-3@HC full cell. Note that the specific capacities were calculated based on the mass of cathode material.

To assess the practical applicability of HEOF-3, a full cell was constructed using HEOF-3 as the cathode and hard carbon (HC) as the anode (the voltage profiles of the hard carbon anode in a half-cell are shown in Fig. S9). As illustrated in Fig. S8a, the HEOF-3@HC full cell demonstrates smooth and inclined plateaus during both charging and discharging processes. The reversible capacities were determined to be 123.65, 123.18, 122.68, 121.22, 121.30, 112.12, 110.94, and 109.94 mAh g⁻¹ in the 1st, 2nd, 3rd, 5th, 10th, 20th, 50th, and 100th cycles, respectively. Notably, the HEOF-3@HC full cell achieved excellent Coulombic efficiencies, approaching 100%, in all cycles except the first, highlighting its exceptional electrochemical reversibility. Furthermore, the cycling stability of the HEOF-3@HC full cell is depicted in Fig. S8b, with a capacity retention of 88.91% after 100 cycles at a current rate of 1C. Collectively, these findings demonstrate that the HEOF-3 cathode is not only viable but also promising for practical applications.

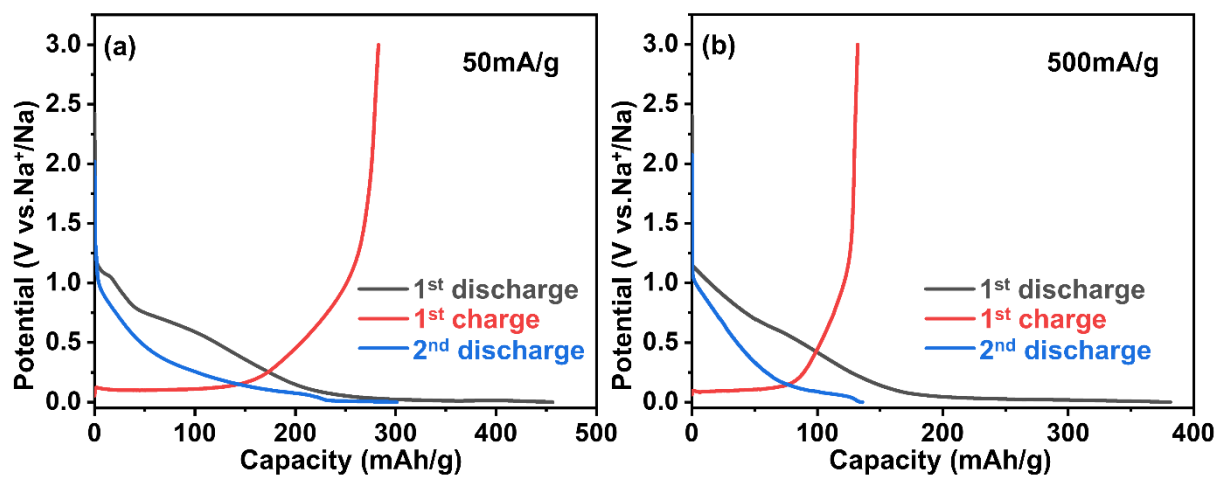


Fig. S9. The initial two charge-discharge curves of hard carbon at current densities of (a) 50 mA g⁻¹ and (b) 500 mA g⁻¹, respectively.

Table S4. Comparison of the electrochemical properties of F-doped Na layered cathode materials.

Electrode materials	Voltage range (V)	Initial reversible capacity (mAh/g)	Capacity at high rate (mAh/g)	Capacity retention After cycling	Reference
$\text{Na}_{0.6}\text{Mn}_{0.95}\text{Ni}_{0.05}\text{O}_{1.95}\text{F}_{0.05}$	1.5-3.5	100.10 (0.1C)	61.94 (5C)	74.0% (200 cycle)	S8
$\text{NaNi}_{1/3}\text{Fe}_{1/3}\text{Mn}_{1/3}\text{O}_{1.99}\text{F}_{0.01}$	2.0-4.0	122 (150 mA g^{-1})	/	90% (150 mA g^{-1} 70 cycle)	S5
$\text{Na}_{0.44}\text{MnO}_{1.93}\text{F}_{0.07}$	2.0-4.2	178 (0.1C)	138 (1C)	83% (1C 150 cycle)	S9
$\text{Na}_{2/3}\text{Ni}_{1/3}\text{Mn}_{2/3}\text{O}_{1.95}\text{F}_{0.05}$	2.0-4.0	106.7 (0.1C)	95.4 (2C)	89% (2C 400 cycle)	S6
$\text{Na}_{0.67}\text{Ni}_{0.33}\text{Mn}_{0.37}\text{Ti}_{0.3}\text{O}_{1.9}\text{F}_{0.1}$	2.0-4.4	140.3(0.1C)	87.7(6C)	77.2% (2C 300cycle)	S10
$\text{Na}_{0.67}\text{Ni}_{0.15}\text{Fe}_{0.2}\text{Mn}_{0.65}\text{F}_{0.05}\text{O}_{1.95}$	1.5-4.3	240(0.1C)	40 (10C)	46.6% (0.1C 50cycle)	S11
$\text{Na}_{0.67}\text{Fe}_{0.1}\text{Mn}_{0.8}\text{Cu}_{0.1}\text{F}_{0.1}\text{O}_{1.9}$	1.5-4.0	195.6(10 mA g^{-1})	141.3 (200 mA g^{-1})	87.8% (200 mA g^{-1} 1200 cycle)	S12
$\text{Na}_{0.67}\text{Ni}_{0.28}\text{Zn}_{0.05}\text{Mn}_{0.62}\text{Ti}_{0.05}\text{O}_{1.95}\text{F}_{0.05}$	2.5-4.35	129 (0.2C)	79.5 (10C)	81.7% (1C 100 cycle)	S13
$\text{Na}_{0.7}\text{Mn}_{0.4}\text{Ni}_{0.3}\text{Cu}_{0.1}\text{Fe}_{0.1}\text{Ti}_{0.1}\text{O}_{1.95}\text{F}_{0.1}$	2.0-4.3	128.4 (20 mA g^{-1})	87 (800 20mA g^{-1})	71.1% (200 mA g^{-1} 200 cycle)	S14
$\text{Na}_{0.65}\text{MnO}_{1.8}\text{F}_{0.2}$	1.9-3.9	124.6(0.1C)	55.9 (10C)	87.9% (2C 500 cycle)	S15
$\text{Na}_{2/3}\text{Ni}_{0.23}\text{Al}_{0.1}\text{Mn}_{2/3}\text{O}_{1.95}\text{F}_{0.05}$	1.5-4.0	125.9 (0.2C)	96 (2C)	86.6% (0.2C 200 cycle)	S16
$\text{Na}_{0.64}\text{Mn}_{0.96}\text{Mg}_{0.04}\text{O}_{1.92}\text{F}_{0.08}$	2.0-4.0	200.88(20 mA g^{-1})	120.26 (1000 mA g^{-1})	79.12% (200 cycle)	S17
$\text{Na}_{0.76}\text{Ni}_{0.23}\text{Li}_{0.1}\text{Ti}_{0.02}\text{Mn}_{0.65}\text{O}_{1.998}\text{F}_{0.02}$	2.0-4.2	110.0(0.1C)	74.8 (10C)	91% (1C 300 cycle)	S18
$\text{Na}_{1.2}\text{Mn}_{0.8}\text{O}_{1.5}\text{F}_{0.5}$	1.5-4.0	174(10 mA g^{-1})	110 (1000 mA g^{-1})	68% (100mA g^{-1} 300 cycle)	S19
$\text{Na}_{0.66}\text{Mn}_{0.6}\text{Li}_{0.1}\text{Ti}_{0.1}(\text{MgAlCuZn})_{0.05}\text{O}_{1.7}\text{F}_{0.3}$	1.5-4.5	177.09 (0.1C)	91.34 (10C)	99.32% (1C, 100 cycles)	This work

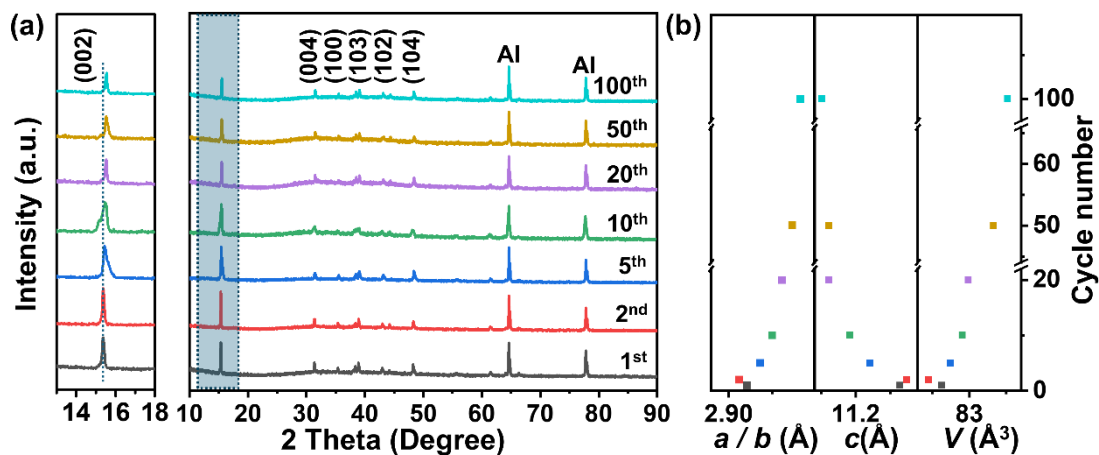


Fig. S10 Structural evolution analysis of the HEOF-3 during 100 cycles. (a) Left: The enlarged view of (002) diffraction peaks in a 2θ range from 13° to 18° . Right: *Ex-situ* XRD patterns of the HEOF-3 collected during 100 cycles at a current rate of 0.1C within voltage range of 1.5-4.5 V vs. Na^+/Na . (d) Evolution of lattice parameters (a , b , c , V) for the HEOF-3 during 100 cycles at a current rate of 0.1C.

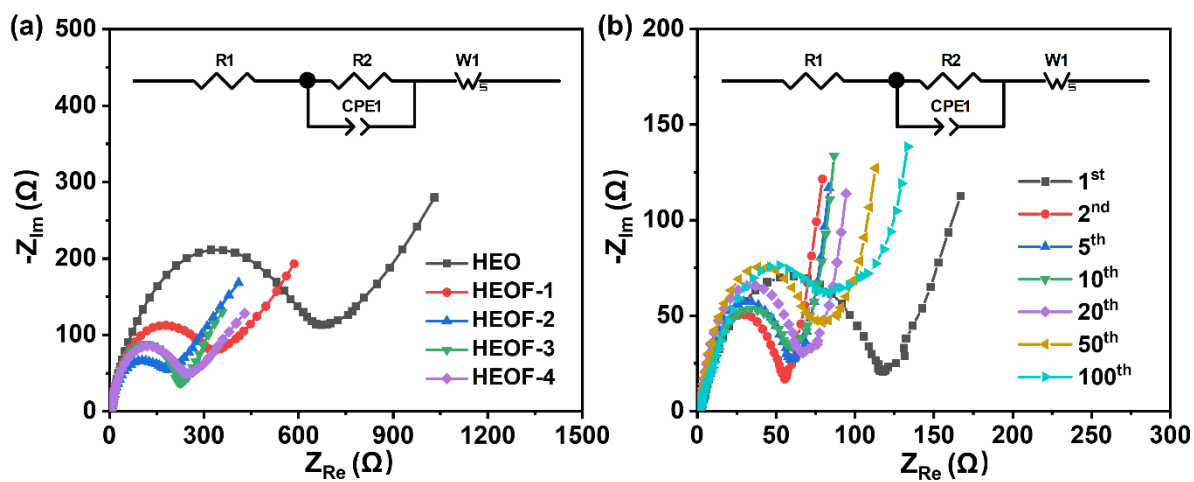


Fig. S11 (a) EIS results of the uncycled HEO, HEOF-1, HEOF-2, HEOF-3 and HEOF-4 electrodes, (b) EIS results of the 1st, 2nd, 5th, 10th, 20th, 50th and 100th cycled HEOF-3 electrode.

Table S5. Fitting results of the impedance parameters and the corresponding ion conductivities of the uncycled HEO, HEOF-1, HEOF-2, HEOF-3 and HEOF-4 electrodes.

Samples	R_e (Ω)	R_{ct} (Ω)	σ (S cm⁻¹)
HEO	6.84	783.17	3.35×10^{-6}
HEOF-1	4.72	419.63	6.24×10^{-6}
HEOF-2	4.58	243.71	1.07×10^{-5}
HEOF-3	2.38	144.94	1.80×10^{-5}
HEOF-4	2.53	181.68	1.44×10^{-5}

Table S6. Fitting results of the impedance parameters and the corresponding ion conductivities of the 1st, 2nd, 5th, 10th, 20th, 50th and 100th cycled HEOF-3 electrode.

Samples	State	R_e (Ω)	R_{ct} (Ω)	σ (S cm⁻¹)
HEOF-3	1 st	2.27	119.94	2.21 × 10 ⁻⁵
	2 nd	1.44	58.62	4.52 × 10 ⁻⁵
	5 th	1.49	66.47	3.99 × 10 ⁻⁵
	10 th	1.54	68.31	3.88 × 10 ⁻⁵
	20 th	1.68	74.75	3.54 × 10 ⁻⁵
	50 th	1.79	89.14	2.97 × 10 ⁻⁵
	100 th	1.96	107.71	2.46 × 10 ⁻⁵

References

- S1 J. Huo, Y. Zhang, W. Kang, Y. Shen, X. Li, Z. Yan, Y. Pan and W. Sun, *Nanoscale Adv.*, 2023, **5**, 2846-2864.
- S2 T. Seaby, T. -E. Lin, Y. -X. Hu, Q. -H. Yuan and L. -Z. Wang, *Rare Metals*, 2022, **41**(6), 1771-1796.
- S3 B. Wang, J. Cui, Z. Li, H. Wang, D. Zhang, Q. Wang, H. Sun and Z. Hu, *J. Alloy Compd.*, 2022, **929**, 167304.
- S4 J. Choi, D. Darbar, M. Chen, X. Huang, G. Qi, L. Wang and J. Kim, *ACS Appl. Energy Mater.*, 2024, **7**(16), 6920-6928.
- S5 Q. Zhang, Y. Huang, Y. Liu, S. Sun, K. Wang, Y. Li, X. Li, J. Han and Y. Huang, *Sci. China Mater.*, 2017, **60**, 629-636
- S6 K. Liu, S. Tan, J. Moon, C. J. Jafta, C. Li, T. Kobayashi, H. Lyu, C. A. Bridges, S. Men, W. Guo, Y. Sun, J. Zhang, M. P. Paranthaman, X. G. Sun and S. Dai, *Adv. Energy Mater.*, 2020, **10**, 2000135.
- S7 H. Ren, Y. Li, Q. Ni, Y. Bai, H. Zhao and C. Wu, *Adv. Mater.*, 2022, **34**(8), 2106171
- S8 H. Chen, Z. Wu, Y. Zhong, T. Chen, X. Liu, J. Qu, W. Xiang, J. Li, X. Chen, X. Guo and B. Zhong, *Electrochimica Acta*, 2019, **308**, 64-73.
- S9 W. -J. Shi, Y. -W. Yan, C. Chi, X. -T. Ma, D. Zhang, S. -D. Xu, L. Chen, X.-M. Wang and S. -B. Liu, *J. Power Sources*, 2019, **427**, 129-137.
- S10 P. Zhou, J. Zhang, Z. Che, Z. Quan, J. Duan, X. Wu, J. Weng, J. Zhao and J. Zhou, *J. Energy Chem.*, 2022, **67**, 655-662.
- S11 X. Cui, S. Wang, X. Ye, X. Fan, C. Gao, Y. Quan, S. Wen, X. Cai, J. Huang and S. Li, *Energy Storage Mater.*, 2022, **45**, 1153-1164.
- S12 Y. Zhang, G. Liu, C. Su, G. Liu, H. Sun, D. Qiao and L. Wen, *J. Power Sources*, 2022, **536**, 231511.
- S13 Y. Fan, X. Ye, X. Yang, L. Guan, C. Chen, H. Wang, and X. Ding, *J. Mater. Chem. A*, 2023, **11**, 3608-3615.
- S14 P. Zhou, Z. Che, J. Liu, J. Zhou, X. Wu, J. Weng, J. Zhao, H. Cao, J. Zhou and F. Cheng, *Energy Storage Mater.*, 2023, **57**, 618-627.
- S15 H. Wang, T. Du, L. Cao, Z. Y. Cheng, L. Y. Liu, Y. S. Wang and L. F. Zhou, *J. Alloy Compd.*, 2024, **1003**, 175741.
- S16 C. Jiang, B. Chen, M. Xu, and J. Jiang, *Energy Storage Mater.*, 2024, **70**, 103518.
- S17 X. Chen, G. Lin, P. Liu, Z. Sun, Y. Si, Q. Wang and L. Jiao, *Energy Storage Mater.*, 2024, **67**, 103303.
- S18 L. Yan, X. Li and H. Pan, *ACS Appl. Mater. Interfaces*, 2024, **16**, 26280-26287.
- S19 B. K. Ganesan and Y. S. Lee, *ACS Appl. Energy Mater.*, 2023, **6**, 960-968.